



Metal–silicate partitioning of Ni and Co in a deep magma ocean

Julien Siebert ^{a,*}, James Badro ^b, Daniele Antonangeli ^a, Frederick J. Ryerson ^{b,c}

^a Institut de minéralogie et de physique des milieux condensés, Institut de physique du Globe de Paris, Univ. Pierre et Marie Curie, UMR 7590 CNRS, Paris, France

^b Institut de Physique du Globe de Paris, France

^c Lawrence Livermore National Laboratory, California, USA

ARTICLE INFO

Article history:

Accepted 11 January 2012

Available online xxxx

Editor: T.M Harrison

Keywords:

Earth's core formation
magma ocean
siderophile elements
light elements
laser-heated diamond anvil cell

ABSTRACT

The pattern of siderophile (iron-loving) element abundance in the silicate portion of the Earth is a consequence of metal separation during core formation. The apparent excess of nickel and cobalt in mantle-derived rocks has been attributed to metal–silicate equilibration in a deep terrestrial magma ocean. Based on the extrapolation of phase equilibria and metal–silicate partitioning results obtained at lower pressure (P) and temperature (T), previous estimates of the P–T of equilibration are all greater than 25 GPa and 3000 K. Using the laser-heated diamond anvil cell, we have extended metal–silicate partitioning measurements for Ni and Co to 75 GPa and 4400 K, exceeding the liquidus temperatures for both metal and silicate (basalt or peridotite) and, therefore, achieving thermodynamic conditions directly comparable to those of the magma ocean. The metal–silicate partition coefficients of nickel and cobalt decrease with increasing pressure and reach the values required to yield present mantle concentrations at ~50 GPa. At these conditions, silicon and oxygen concentrations measured in the metallic liquid allow to solve the seismically constrained core density deficit. Above 60 GPa, the partition coefficients become too low, resulting in an overabundance of Ni and Co in the silicate mantle. Our data therefore support the paradigm of core formation in a deep magma ocean, providing an upper bound for the depth at which Earth's core may have formed, and explaining the main geophysical (density) and geochemical (excess siderophile elements) observables.

© 2012 Elsevier B.V. All rights reserved.

1. Introduction

Extensive melting of the proto-Earth is supported by its violent accretion history with impacts being the main energy source (e.g. Halliday and Wood, 2009; Tonks and Melosh, 1993). Other factors, such as gravitational energy due to core segregation, radiogenic heating by short-lived isotopes (²⁶Al, ⁶⁰Fe), and thermal blanketing effects of a dense primitive atmosphere also likely contributed in raising mantle temperatures, resulting in substantial melting and formation of a terrestrial magma ocean (Matsui and Abe, 1986; Safronov, 1978; Stevenson, 1990). Gravitational separation of immiscible silicate and metallic melts, along with fractionation of silicate minerals, in the magma ocean plays a fundamental role in determining the large-scale chemical differentiation of the Earth. Following Stevenson (1990), the simplest core formation scenario is a single-stage core formation in which molten metal sinks through the magma ocean, ponding at the top of a solid underlying proto-mantle. The depth and temperature at this rheological boundary, which are necessarily constrained by the mantle solidus, correspond to the last P–T conditions at which silicate and metal are in chemical equilibrium. Subsequent descent of metal diapirs through the solid silicate mantle is thought to be too rapid and

diffusion distances too long to maintain equilibrium between the metallic melt and surrounding silicate.

Mass balance calculations using trace element constraints on the bulk Earth (chondrites) and residual magma ocean (modern upper mantle) can be used to infer an integrated “core–mantle” partition coefficient and provide a fundamental constraint on all core formation scenarios. For single-stage core formation, comparison of this observed core–mantle partitioning and experimental metal–silicate partitioning, obtained over a range of P–T, can therefore provide an estimate of magma ocean depth. Single-stage core formation requires that identical P–T coordinates be recovered for each element considered and that this P–T condition agree with the locus of the peridotite solidus–liquidus interval. That numerous investigators have been unable to obtain a consistent P–T solution for a broad range of siderophile elements (Siebert et al., 2011; Wade and Wood, 2005; Wood et al., 2008), based on partitioning data obtained at P ≤ 25 GPa, has called for more complex scenarios invoking variable P–T–fO₂ conditions accompanying accretion and metal–silicate equilibration (Wade and Wood, 2005), or the addition of a late veneer contribution (e.g. Brenan and McDonough, 2009). Furthermore, the depth of the magma ocean is also expected to play a crucial role in fixing the concentration of light elements present in the core. Formulation of models that can satisfy both light element concentrations in the core and siderophile trace-element concentrations in the mantle remains a major issue in terrestrial geodynamics.

* Corresponding author at: IMPMC, UMR CNRS 7590, 4 place jussieu, campus jussieu, Boîte courrier 115, 75252 Paris Cedex 05, France. Tel./fax: +33 1 44 27 98 19/37 85.

E-mail address: julien.siebert@impmc.jussieu.fr (J. Siebert).

Ni and Co are refractory elements that undergo very limited volatilisation, so their abundance patterns are largely controlled by core formation alone. The nearly chondritic Ni/Co ratio in the upper mantle requires that $D_{\text{Ni}}^{\text{met-sil}} \sim D_{\text{Co}}^{\text{met-sil}}$ during metal–silicate equilibration. At one-atmosphere $D_{\text{Ni}}^{\text{met-sil}}$ is more than an order of magnitude larger than $D_{\text{Co}}^{\text{met-sil}}$, and as suggested by Li and Agee (1996), the convergence of both partition coefficients may be a direct consequence of core–mantle equilibration at high pressure. While the addition of a late-stage chondritic veneer subsequent to core formation has been invoked to raise the concentrations of highly siderophile elements (e.g. PGEs) to their observed values (e.g. Brenan and McDonough, 2009; Holzheid et al., 2000), this mechanism has a negligible effect on Ni and Co concentration in the primitive mantle. Hence a great deal of effort has been dedicated to determining their partitioning between metal and silicate liquids over the range of P–T conditions attainable in large volume, multi-anvil presses (up to 25 GPa and 2700 °C) to determine the P–T conditions at which $D_{\text{Ni}}^{\text{met-sil}}$ and $D_{\text{Co}}^{\text{met-sil}}$ converge (e.g. Chabot et al., 2005; Gessmann and Rubie, 2000; Li and Agee, 1996; Li and Agee, 2001; Righter et al., 1997; Siebert et al., 2011; Thibault and Walter, 1995; Wade and Wood, 2005). Among these, however, only a recent study by Bouhifd and Jephcoat (2011) was conducted at high enough pressures to produce a silicate melt with mantle Ni/Co signature. Other investigators have relied on the extrapolation of low pressure results to more extreme conditions, yielding disparate estimates for the base of the magma ocean (Bouhifd and Jephcoat, 2003; Chabot et al., 2005; Corgne et al., 2009; Gessmann and Rubie, 2000; Li and Agee, 1996; Li and Agee, 2001; Righter, 2011; Righter et al., 1997; Siebert et al., 2011; Wade and Wood, 2005), ranging from 25 to 60 GPa and 2000 °C to over 3800 °C. Moreover, recent results (Kegler et al., 2008) state for a weaker pressure effect on Ni and Co partitioning above 3–5 GPa. Such effect, ascribed to a structural change in silicate melts at this P condition, questions the possibility of producing a chondritic Ni/Co ratio by single stage core–mantle equilibration at the bottom of a magma ocean under any P–T conditions. Such discrepancies highlight the need for additional direct measurements of Ni and Co partitioning at very high P–T. The laser-heated diamond anvil cell (LH-DAC) is the only static pressure tool capable of producing these conditions, but its capabilities for synthesizing materials suitable for quantitative metal–silicate chemical analyses at extreme conditions have been hindered by series of technical hurdles linked to sample recovery, analyses at small spatial scales, and chemical equilibrium.

Here we report the measurement of Ni and Co partitioning between metal and silicate at super-liquidus conditions using the LH-DAC to pressures and temperatures of 75 GPa and 4400 K. A focused ion beam instrument (FIB) was used to recover thin sections from the samples quenched from extreme P–T conditions, and electron microprobe analyses to obtain major and trace element concentrations.

2. Experimental methods

2.1. Starting material

2.1.1. Silicate

Two different silicate starting materials were used in these experiments: a natural olivine tholeiite basalt (Kilauea, Hawaii), and a synthetic peridotite (KLB-1 composition); both were doped with high-purity NiO and CoO oxides and transformed into a glass using a levitation device coupled with a CO₂ laser (Auzende et al., 2011). Spherical samples with diameters ~2 mm are aerodynamically levitated using an argon gas flow coming from below the sample and melted with a continuous 120 W CO₂ laser. The temperature is measured using an optical pyrometer in the 350–3000 °C range. Backscattered electron images and WDX analyses (15 kV, 20 nA) of the products (Table 1) confirmed the fully vitreous state of the samples and their chemical homogeneity.

2.1.2. Metal

We used foils of either pure iron (10 µm thickness) or silicon bearing iron–nickel alloy to lower the oxygen fugacity of the experiments. Silicon-bearing, iron–nickel alloy was prepared following Antonangeli et al. (2010) at 10 kbars and 1850 °C in a piston cylinder apparatus at the Lawrence Livermore National Laboratory, using a standard 1/2" BaCO₃ pressure cell assembly, with a graphite furnace and a MgO capsule. The starting material consisted in homogenized mixture of high purity metallic and oxide powders of Fe, Si, Ni and SiO₂, with a 60 wt.% metallic portion relative to oxide. Partial oxidation of silicon metal is a critical issue in the synthesis of silicon-rich iron alloy and can lead to SiO₂ exsolution in the iron alloy. The superliquidus melting conditions used here result in segregation of SiO₂ glass from a Fe–Ni–Si metallic blob free of SiO₂ inclusions. The recovered metallic blob, about 1 mm diameter, was polished and analyzed with an electron probe micro-analyzer operating at 20 kV and 50 nA. Multiple analyses as well as backscattered electron images show homogenous Fe–Ni–Si alloy composition without quench textures at the scale of imaging and analytical resolution. Silicon and nickel concentrations are 7.3 wt.% and 4.3 wt.%, respectively. The sample was manually polished to a thickness of 10 µm for loading in the diamond anvil cell.

2.2. Diamond anvil cell experiments

High-pressure high-temperature experiments were conducted using diamond anvil cells (300 µm culet anvils) coupled with a laser-heating system at IMPMC-IPGP (Paris, France) and at the high-pressure beam station ID27 of the ESRF (Grenoble, France). Experimental conditions and results are summarized in Table 2. A metal foil (surface of about 20 µm²) of pure Fe or Fe–Ni–Si alloy was sandwiched between two layers of silicate glass loaded in a drilled rhenium gasket, pre-indented to 25 µm thickness with a 125 µm hole diameter. The silicate glass layers acted as the pressure medium and as a thermal and chemical insulator. A small ruby ball was placed on the surface of one diamond for pressure calibration in a location remote from the heated zone to avoid chemical interaction with the silicate melt. Samples were heated from both sides at high pressure by focusing a high-power continuous fiber laser ($\lambda = 1070$ nm, 100 W). We either split a single laser into two separate beams with equivalent power and orthogonal polarization axis (IMPMC-IPGP) or used two lasers (ESRF) to heat the sample from both sides, minimizing the thermal gradients. Temperature was measured by the spectro-radiometric technique (Boehler, 2000) in the spectral range 500–750 nm. The thermal emission from both sides of the heated sample was analyzed with a single-stage monochromator and collected on a cooled CCD detector. Temperatures, measured continuously (every 3 s) from both sides simultaneously during the entire duration

Table 1

Electron probe microanalyses of silicate glass starting materials synthesized by laser levitation device.

Wt.%	Tholeiite basalt	Peridotite-KLB1
MgO	9.38 (0.08)	37.10 (0.22)
SiO ₂	47.70 (0.13)	43.06 (0.20)
Al ₂ O ₃	12.59 (0.10)	3.53 (0.04)
FeO	10.67 (0.19)	7.44 (0.18)
CaO	10.83 (0.07)	3.55 (0.06)
Na ₂ O	0.58 (0.03)	0.02 (0.01)
K ₂ O	0.14 (0.01)	–
TiO ₂	2.83 (0.04)	–
NiO	0.77 (0.06)	0.25 (0.05)
CoO	0.71 (0.05)	0.46 (0.04)
MnO	0.49 (0.05)	1.08 (0.06)
V ₂ O ₃	0.18 (0.03)	0.14 (0.03)
Cr ₂ O ₃	0.30 (0.03)	0.22 (0.03)
Nb ₂ O ₃	0.69 (0.15)	0.47 (0.09)
Total	97.87 (0.32)	97.32 (0.40)

Table 2
Experimental summary.

Run #	Fox1	X2-2	X1-2	X1-3	X1-4	X2-4
P, T conditions	62 GPa 4300 K	48 GPa 3100 K	71 GPa 3500 K	35 GPa 3300 K	50 GPa, 3700 K	74 GPa 4400 K
Run duration	3 min	45 s	1 min	40 s	1 min	40 s
Starting materials metal, silicate	Pure Fe, basalt	(Fe, Ni, Si), basalt	(Fe, Ni, Si), basalt	(Fe, Ni, Si), basalt	(Fe, Ni, Si), peridotite	(Fe, Ni, Si), basalt
fO_2 (ΔIW) ^a	–0.92	–1.07	–1.26	–0.83	–1.35	–0.60
$\text{Log}K_D^{\text{Ni}}$ ^b	0.116 (0.004)	0.348 (0.003)	0.005 (0.006)	0.428 (0.005)	0.346 (0.069)	0.112 (0.015)
$\text{Log}K_D^{\text{Co}}$	0.129 (0.003)	0.292 (0.002)	0.063 (0.008)	0.386 (0.018)	0.242 (0.070)	0.039 (0.018)
$\text{Log}K_D^{\text{Si}}$	–2.101 (0.002)	–2.834 (0.004)	–2.137 (0.008)	–1.798 (0.002)	–1.924 (0.050)	–1.214 (0.024)
$\text{Log}K_D^{\text{Fe}}$ ^c (for peridotite)	–2.523	–3.230	–2.579	–2.074	–1.922	–1.632
$\text{Log}K_D^{\text{O}}$ ^d	–0.145 (0.015)	–0.308 (0.020)	–0.271 (0.015)	–0.351 (0.029)	–0.024 (0.078)	–0.094 (0.051)

^a Oxygen fugacity (fO_2) was calculated relative to the iron-wüstite (IW) equilibrium ($\text{Fe} + \frac{1}{2}\text{O}_2 = \text{FeO}$) by assuming that the activities of Fe (a_{Fe}) and FeO (a_{FeO}) in the metal and silicate were equal to their mole fractions. Using a non ideal mixing model for a_{Fe} and a_{FeO} would increase the fO_2 by a maximum of 0.4 log units if γ_{Fe} is calculated with the interaction parameters approach (Siebert et al., 2011; Wade and Wood, 2005) and taking a value of 1.5 for γ_{FeO} in silicate melt.

^b $K_D^M = \frac{x_{\text{metal}}^{\text{metal}}}{x_{\text{silicate}}^{\text{silicate}}} \frac{D_M}{(D_{\text{Fe}})^{1/2}}$ with x the molar fractions and D the molar metal–silicate partition coefficients ($M = \text{Ni, Co, Si}$).

^c Values for $\text{Log}K_D^{\text{Si}}$ are corrected for a peridotite composition after Corgne et al. (2008).

^d $K_D^{\text{O}} = \frac{x_{\text{metal}}^{\text{metal}} - x_{\text{silicate}}^{\text{silicate}}}{x_{\text{silicate}}^{\text{silicate}} - x_{\text{FeO}}^{\text{FeO}}}$ (assuming the following exchange reaction for oxygen: $\text{FeO}_{\text{silicate}} = \text{Fe}_{\text{metal}} + \text{O}_{\text{metal}}$).

of the experiment, were obtained by fitting the thermal radiation spectrum to Planck's function with an uncertainty around ± 150 K (Boehler, 2000; Fiquet et al., 2010). Temperature was quickly ramped to target temperature, and run durations ranged between 40 s to 3 min. The quoted temperature of the runs corresponds to the average of the monitored temperature from both sides. A typical heating cycle is shown on Fig. 1 that displays the measured temperatures during run X1-2 (71 GPa–3500 K). The samples were quenched by cutting off the laser power, thus providing high-cooling rates.

Pressure was measured at room temperature, before and after heating, using the ruby fluorescence technique. An experiment (Fox1) was conducted at beamline ID27 of the European Synchrotron Radiation Facility (ESRF), carrying out high P–T X-ray diffraction measurements (33 keV) from which thermal pressure at 3600 K was determined to be 9 GPa from the cell parameters of the magnesium perovskite (Mg,Fe) SiO_3 using a thermal equation of state for KLB-1 peridotitic starting material (Ricolleau et al., 2009). This leads to a

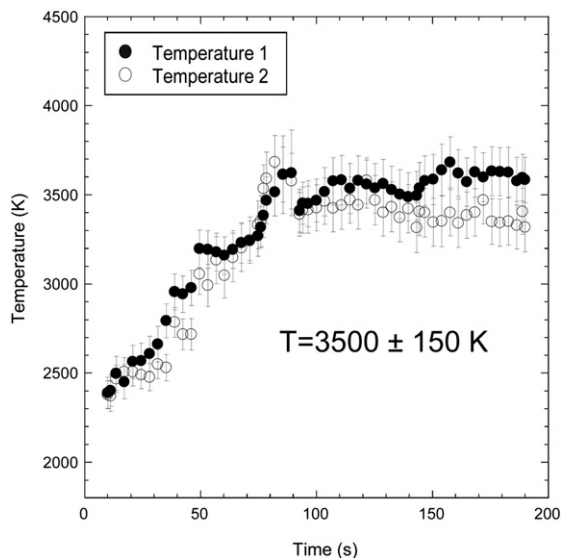


Fig. 1. Temperatures recorded simultaneously from both sides of the sample during experiment X1-2 (71 GPa, 3500 K). The quoted temperature of the runs corresponds to the average of the monitored temperature from both sides. Displayed error bars correspond to an estimate of the uncertainty of the spectral temperature measurement according to Benedetti and Loubeyre (2004); the intrinsic precision of the fits is better than 10° .

value of $\Delta P_{\text{th}} \sim 2.7^{-3}$ GPa/K in good agreement with in situ X-ray experimental work results (Fiquet et al., 2010) where, for similar run conditions, thermal pressure is estimated as 10–19% of the initial pressure value. Following Andraut et al. (1998), the effective thermal pressure corresponds to about half of theoretical thermal pressure $\Delta P_{\text{th}} = \alpha K \Delta T$ (where α and K are the thermal expansion and bulk modulus respectively). This leads to a similar value of $\Delta P_{\text{th}} \sim 2.510^{-3}$ GPa/K using the thermo-elastic parameters of Mg-perovskite (main silicate component). Additionally, Andraut et al. (2011) reports similar values for thermal pressures estimated using the thermo-elastic parameters of Ca-perovskite. In all other experiments the pressure obtained by ruby fluorescence was corrected for thermal pressure.

2.3. Sample recovery and analytical methods

2.3.1. Focused ion beam

The laser-heated region was clearly distinguishable ($\sim 30 \mu\text{m}$ diameter circular surface bump) by electron or optical microscopy (Fig. 2) and thin section was recovered using a crossbeam Focused Ion Beam (FIB) milling system (Neon, Zeiss) at IMPMC (Paris, France). First, a platinum strip was deposited on the center part of the heated zone to protect the top of the sample from gallium beam damage and gallium contamination. The cut is made along the axis of compression, through the hot spot and over the entire thickness of the DAC sample (~ 15 – $20 \mu\text{m}$) with a gallium beam operating at 30 kV and 20 A–50 pA for final surfacing. The crossbeam FIB provides electron images during the milling that allows careful selection of the region of interest, characterized by the coexistence of metal and silicate liquids formed in the hot spot. Relatively large sections (~ 20 – $30 \mu\text{m}$ and 2– $4 \mu\text{m}$ thick) were recovered from the rhenium gasket in situ with a needle from the rhenium gasket and welded to a copper grid for further polishing and transfer to other micro-analytical instruments (Fig. 2). Axial thermal gradients in these samples are limited as seen on Figs. 2 and 3 where a large fraction of the sample is kept above the liquidus along the cross-section.

2.3.2. Electron probe micro-analysis (EPMA)

Metal and silicate phases of the run products are large enough ($> 5 \mu\text{m}$) to perform reliable analyses with the EPMA (Table 3a, 3b). Metal and silicate phases were analyzed using a Cameca SX100 (Paris) and JEOL JXA-8200 (LLNL) electron probe micro-analyzers. X-ray intensities were reduced using the CITZAF correction routine (Armstrong, 1995). Operating conditions were 15 kV accelerating voltage, and 10–20 nA beam current and counting times of 10–20 s

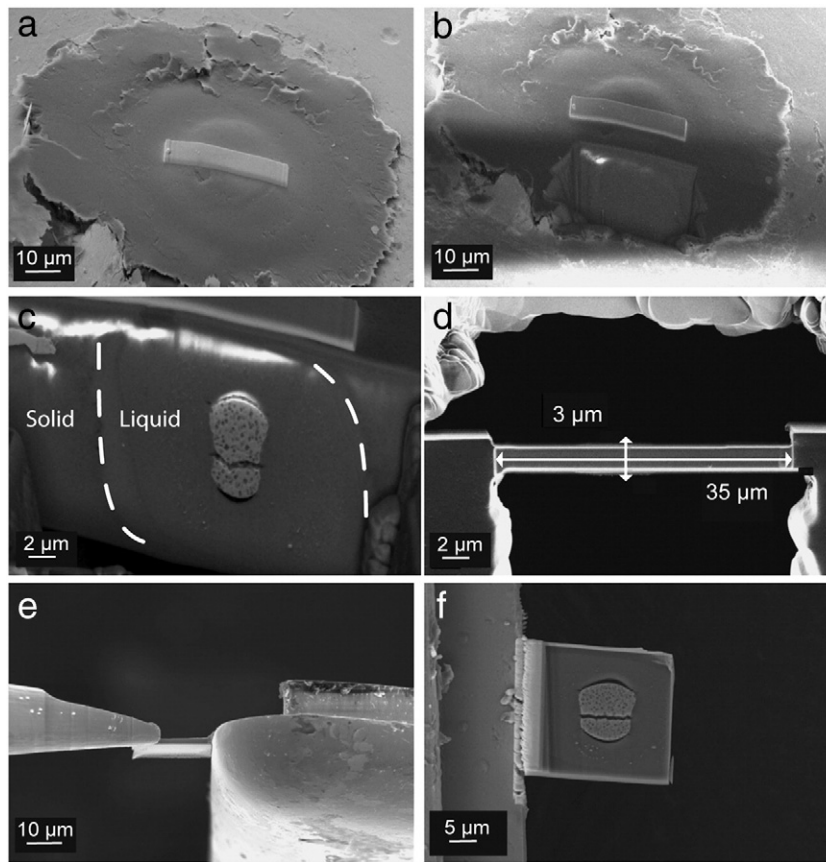


Fig. 2. Electron images of the procedure for sample recovery using the focused ion beam system (FIB). (a) The platinum coating is deposited at the center of the heated zone to protect the sample from Ga contamination. (b) The section is cut over the entire thickness of the sample (thickness of the rhenium gasket 15–20 μm) to constrain the geometry of the molten region. (c) Overview of the section with coexistence of quenched metal and silicate. (d) The section is imaged at 0° to measure its thickness. (e) The section is removed from the gasket by a tungsten needle. (f) Overview of the final sample. The section has been fixed to a copper grid by platinum welding before final polishing at lower current conditions (50–100 pA).

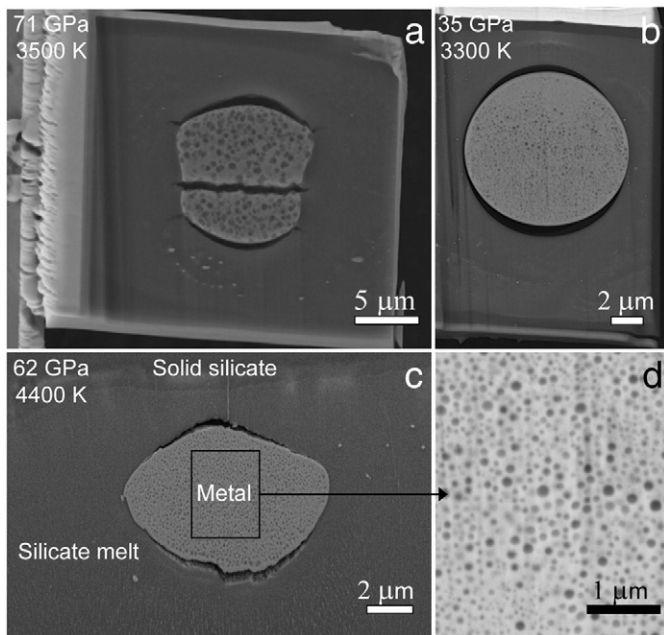


Fig. 3. Backscattered electron images of samples recovered from high P–T, LH-DAC experiments. Metal (white) and silicate melts (gray) are well separated in all run products indicative of super-liquidus conditions. The dark rims surrounding the quenched metal blobs are either cracks due to decompression of the samples (a, c) or topographic effects due to differential FIB polishing of the metal and silicate (b). Contrast between molten silicate (light gray) and surrounding silicate/oxide (dark gray) phases indicates iron enrichment in the melt (c). Metallic and silicate liquids quenched to heterogeneous textures with Si–O rich exsolutions in the metal (a, b, c, d).

on peak and background for major elements and 20–40 s for Ni and Co. Pure Fe metal was used as standard for metal. Fe_2O_3 and SiO_2 were used as standards to measure solubility of oxygen and silicon in metal. Diopside glass (Si), wollastonite (Ca), orthoclase (K), anorthite (Al), albite (Na), rutile (Ti) and pure oxides (Fe_2O_3 , MgO, SiO_2 , CaO and Al_2O_3) were used as standards for the silicate. Pure metals Ni and Co were used as standards for both silicate and metal. Corrections for possible interference between Fe and Co was applied using a working curve determined from Co-free standards. The cylindrical geometry of metal and silicate phases was observed from both sides of the thick FIB sections (2–4 μm); the excitation volume of EPMA analyses is therefore confined to a single metal or silicate phase. Post-run oxidation of the metal was checked by preparing a similar FIB section in a pure-iron foil. No oxygen was detected by EPMA on the sample showing that post-run oxidation of iron metal is below detection limit.

EPMA analyses with 1–2 μm beam size are large enough to integrate the small quench features of metal and silicate phases (<200 nm) and determine their bulk compositions. Occasionally, small metallic droplets (about ~500 nm to 2 μm diameter) were trapped in the silicate upon quench, before coalescing with the main central molten iron blob. These particles were avoided during analysis. There are several lines of evidence demonstrating that achievement of equilibrium was approached in these runs: (1) Compositional homogeneity of silicate and metal phases and small standard deviations of electron microprobe analyses shown in Table 3a and 3b support the approach to equilibrium. (2) The fact that partitioning behavior is consistent with a thermodynamic model, including the large existing dataset at lower P–T conditions, is also an argument for having achieved equilibrium conditions. (3) Time-series and chemical reversal experiments demonstrated that at

Table 3a

Electron probe microanalyses of the quenched silicate melts.

Run #	Fox1	X2-2	X1-2	X1-3	X1-4	X2-4
P (GPa)	62	48	71	35	50	74
T (K)	4300	3100	3500	3300	3700	4400
MgO	7.75 (0.08)	8.45 (0.12)	9.94 (0.42)	8.43 (0.22)	30.67 (2.15)	6.94 (0.46)
SiO ₂	31.93 (0.65)	33.56 (0.81)	37.74 (1.50)	36.52 (0.76)	39.99 (1.20)	38.23 (1.89)
Al ₂ O ₃	18.51 (0.39)	16.68 (0.34)	17.77 (0.35)	9.26 (0.18)	4.62 (0.34)	13.51 (0.56)
CaO	3.03 (0.08)	3.44 (0.11)	3.95 (0.97)	5.17 (0.18)	3.29 (0.20)	3.10 (0.11)
Na ₂ O	0.55 (0.03)	1.24 (0.03)	0.79 (0.12)	0.61 (0.02)	–	0.53 (0.04)
K ₂ O	0.15 (0.10)	0.35 (0.01)	0.13 (0.00)	0.15 (0.02)	–	0.13 (0.01)
FeO	27.20 (0.90)	24.91 (1.11)	20.83 (0.70)	31.52 (0.51)	18.25 (1.93)	26.03 (2.75)
TiO ₂	4.32 (0.20)	3.51 (0.06)	3.08 (0.03)	2.98 (0.10)	–	3.82 (0.09)
NiO	1.21 (0.11)	1.38 (0.11)	1.46 (0.16)	1.15 (0.12)	0.37 (0.13)	1.23 (0.18)
CoO	0.61 (0.04)	0.51 (0.02)	0.48 (0.06)	0.20 (0.04)	0.05 (0.02)	0.29 (0.05)
Total ^a	99.04 (1.12)	97.36 (0.61)	98.58 (1.91)	97.77 (0.57)	99.80 (1.24)	96.32 (1.39)

^a Totals also include trace elements that concentrations are not reported.

5 GPa and $T > 2300$ K equilibrium partitioning of Ni, Co and Fe is accomplished in less than 5 s (Corgne et al., 2008; Thibault and Walter, 1995). These observations indicate that the diffusion coefficients for siderophile elements in liquid Fe alloy and liquid silicate are much larger than $10 \mu\text{m}^2/\text{s}$ under these conditions. Heating duration at superliquidus conditions in the present experiments was 30 s to 3 min. This is much longer than the few seconds sufficient to reach chemical equilibrium.

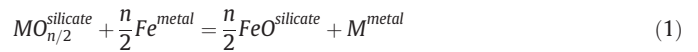
The possibility of carbon diffusion from the diamonds into the metal was also assessed. A calibration curve for the $C_{K\alpha}$ line intensity was established using standards containing 0, 0.92, and 2.94 wt.% carbon. Measured carbon contents were below the detection limits (estimated around 1 wt.%).

3. Results

Most of the experiments were conducted with basaltic compositions at temperatures above or at the liquidus of peridotite (Andrault et al., 2011; Fiquet et al., 2010). Basalt has a lower melting point than peridotite so that the experiments in this study are all in superliquidus (fully molten) conditions. This is further confirmed by the standard experimental petrological method of analyzing quench texture: in all runs, silicate and metal display textures characteristic of quenched liquids (see backscattered images in Fig. 3). We also observed discontinuities (plateaus) in the power versus temperature function due to a change in the absorption of the laser with presence of liquid sample followed by a sharp increase in temperature when a threshold of liquid volume fraction is reached. This has been used as a melting criterion and for the determination of the liquidus in previous experimental work (Andrault et al., 2011; Fiquet et al., 2010; Lord et al., 2009). Finally, X-ray diffraction patterns collected on experiment Fox1 at ESRF at the center of the hot spot display diffuse scattering liquid contribution and decrease of diffraction peaks intensity due to the presence of liquid.

Metallic liquids exhibit heterogeneous texture due to the presence of a Fe–Si–O-rich phases that exsolved during quench (Fig. 3). Such features in the metal have often been observed in large volume press (O'Neil et al., 1998; Ricolleau et al., 2011) or DAC (Frost et al., 2010) partitioning experiments. The silicate melt was enriched in FeO relative to starting material, by roughly a factor of 3 (see Tables 2 and 3a, 3b). This is likely a consequence of preferential partitioning of FeO in the melt (with respect to the surrounding solid silicate). This has been observed in numerous studies, and melt/solid silicate partitioning experiments report values from 2 to 3 for Fe partitioning in favor of the melt (e.g. melt/Mg-perovskite partitioning experiments (Corgne et al., 2005; Nomura et al., 2011)). The presence of excess FeO renders the redox conditions of the experiments more oxidizing than expected ($-0.6 < \Delta\text{IW} < -1.4$).

The partitioning of a siderophile element M (Ni or Co) between metal and silicate is described by the reaction,



where n is the valence of the cation M in the silicate melt.

At equilibrium for a given P and T, the Ni and Co metal/silicate partition coefficient $D_M^{\text{met-sil}}$, is the ratio of the concentration of M in the metal over that in the silicate. The exchange coefficient $K_D^M = \frac{D_M}{D_{Fe}}$, derived from reaction (1), is the molar ratio of partition coefficients D_M and D_{Fe} . Thus, the partition coefficients are normalized to iron partitioning allowing experimental data to be compared independently of oxygen fugacity. Given D_{Fe} for the Earth of 13.6, D_{Ni} between 24 and 28, and D_{Co} between 23 and 26 (Allège et al., 1995; McDonough, 2003; Palme and O'Neill, 2003), values of $\log K_D$ equal to 0.25–0.31 for Ni and 0.23–0.28 for Co are required to obtain Ni and Co concentrations in the bulk silicate Earth (BSE) by core formation.

Table 3b

Electron probe microanalyses of the metallic melts.

Run #	Fox1	X2-2	X1-2	X1-3	X1-4	X2-4
P (GPa)	62	48	71	35	50	74
T (K)	4300	3100	3500	3300	3700	4400
O	8.33 (0.09)	4.24 (0.02)	3.70 (0.29)	5.33 (0.33)	6.82 (0.41)	17.00 (0.80)
Fe	77.11 (0.38)	74.51 (0.45)	74.20 (1.49)	76.15 (1.61)	77.56 (0.56)	64.58 (1.37)
Si	1.24 (0.02)	0.30 (0.00)	2.51 (0.27)	2.19 (0.09)	5.79 (0.18)	6.87 (0.67)
Mg	–	–	0.19 (0.13)	0.08 (0.02)	0.46 (0.06)	0.35 (0.04)
Co	2.37 (0.02)	3.01 (0.00)	2.01 (0.04)	1.18 (0.08)	0.34 (0.02)	0.81 (0.04)
Ni	4.52 (0.03)	9.29 (0.00)	5.34 (0.13)	7.54 (0.26)	3.58 (0.11)	3.98 (0.12)
Total ^a	95.71 (0.35)	95.41 (0.12)	92.95 (2.99)	94.21 (2.05)	96.81 (0.39)	95.82 (0.84)

^a Totals also include trace elements that concentrations are not reported.

As observed in previous investigations at lower pressure, Ni and Co become less siderophile with pressure, $D_{\text{Ni}}^{\text{met-sil}}$ and $D_{\text{Co}}^{\text{met-sil}}$ decreasing with pressure between 35 and 75 GPa (Fig. 4). Most importantly, the experimentally determined values of $D_{\text{Ni}}^{\text{met-sil}}$ and $D_{\text{Co}}^{\text{met-sil}}$ become equal to the “core–mantle target” at about 50 GPa, and dip below the required values for core–mantle equilibration above 60 GPa. This direct observation establishes an upper limit of 60 GPa for core–mantle equilibrium during a single stage event. Had final core–mantle equilibrium occurred at higher pressures, the present-day mantle would be enriched in Ni and Co. In the pressure and temperature range of our experiments, the effect of

temperature on partitioning is not significant (Fig. 4). At pressures above 60 GPa, we report negligible dependence of exchange coefficients between 3500 and 4400 K. This is consistent with previous work showing that temperature effects are pressure dependent and become smaller at pressures above 10 GPa for both Ni and Co (Kegler et al., 2008; Wade and Wood, 2005). Contrary to their conclusions, when normalized to iron partitioning, the results obtained between 40–52 GPa and 3150–3480 K by Bouhifd and Jephcoat (2011) are not in agreement with the observed core–mantle partition coefficients (Fig. 4). This is especially true for Co while data for Ni show a relatively good agreement with data from this work.

Along with Ni and Co, we observed significant quantities of Si and O in the metal (Table 3a, 3b). The solubility of these light elements in metal is greatly enhanced by increasing temperature while the effect of pressure seems negligible to first order (Fig. 5). Redox conditions

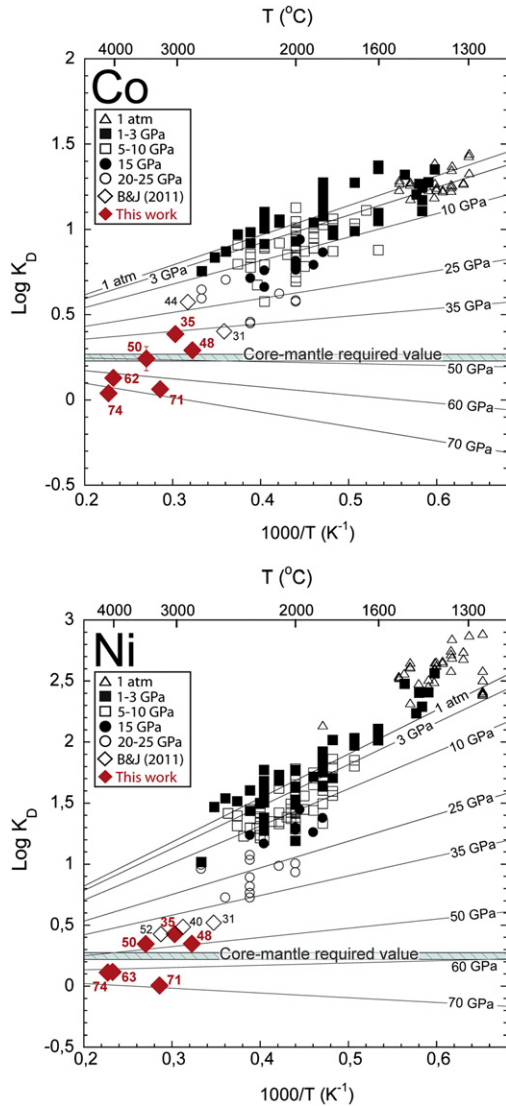


Fig. 4. Exchange (i.e. Fe-normalized) coefficients (K_D) for Co and Ni plotted as a function of reciprocal temperature: this work (red diamonds with labeled pressure conditions), DAC experiments by Bouhifd and Jephcoat (2011) (only above 30 GPa, white diamonds with labeled pressure conditions) and other studies (refs. Capobianco et al., 1999; Chabot et al., 2005; Corgne et al., 2008; Hilgren et al., 1996; Kegler et al., 2008; Li and Agee, 2001; Ohtani et al., 1997; Siebert et al., 2011; Thibault and Walter, 1995; Wade and Wood, 2001, 2005) at different pressure conditions. Our data, obtained with the diamond anvil cell, provide direct experimental verification that required Ni and Co abundances in the mantle (shaded horizontal interval) can be produced from high P–T metal–silicate equilibrium in a deep magma ocean. Data above 60 GPa are below the required Ni and Co targets for the mantle, providing an upper limit for pressure and depth of single-stage core–mantle equilibrium. Solid lines, calculated at different pressures, are based on regression fits for Ni and Co partitioning for data from experiments conducted above 5 GPa (Eqs. (3) and (4)).

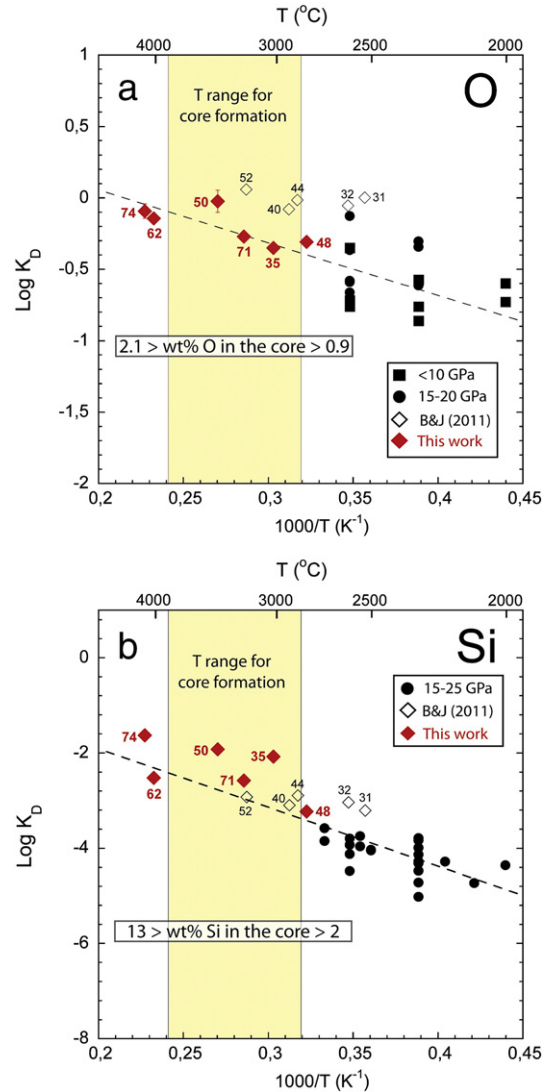


Fig. 5. Exchange coefficients (K_D) for O and Si plotted as a function of $1000/T$: this work (red filled diamonds with labeled pressure conditions), DAC experiments by Bouhifd and Jephcoat (2011) (only above 30 GPa, white diamonds with labeled pressure conditions) and other studies (Ito et al., 1995; Li and Agee, 2001; Mann et al., 2009; Ricolleau et al., 2011; Wade and Wood, 2001, 2005) conducted at lower pressures. To limit the influence of compositions, results for comparison were restricted to experiments (1) with silicate melts, (2) without high sulfur contents in the iron metal, and (3) performed in MgO capsules. All K_D for Si are corrected for a peridotite melt composition using the parameterization given in Corgne et al. (2008). Assuming that the K_D s are not oxygen fugacity dependent, we infer the possible amounts of oxygen and silicon into the core by considering a mantle with 8 wt.% FeO and a core with 85 wt.% Fe.

(and hence the nature of the accretionary material) have a large influence on Si and O solubility as the FeO content of the silicate melt dramatically affects O and Si partitioning between metal and silicate. Solubility of oxygen in experiment X1–4 at lower oxygen fugacity conditions is higher than predicted from the regression of the available dataset (Fig. 5). This may be attributed to a non-linear effect of FeO content in silicate melt on partitioning, as recently reported for metal–magnesiowüstite equilibrium (Frost et al., 2010). Also, interactions between oxygen and silicon in the Fe–Si–O metallic system make simultaneous oxygen and silicon solubility in the liquid metal energetically favorable (Japan Society and the Promotion of Science and the Nineteenth Committee on Steelmaking, 1988), and could explain the observation of a high O and Si solubility. However, this issue requires additional experiments to be properly addressed.

4. Discussion

Assuming that Ni and Co partitioning is independent of silicate and metal composition (e.g. Jana and Walker, 1997; Siebert et al., 2011), partitioning follows the thermodynamic relation:

$$\log K_D = a + \frac{b}{T} + \frac{c \cdot P}{T} \quad (2)$$

where a , b , and c are constants, P is pressure and T temperature. Combining our measured K_D with those of previous studies performed at lower P – T conditions we obtain a , b , and c from least squares multi-variable regression (Table 4). A single regression including literature data below 5 GPa does not provide an adequate fit to the high-pressure data of this work. Regressions including low pressure data (<3 GPa) typically underestimate $\log K_D$ for Ni and Co at high pressure whereas a single regression without considering data below 5 GPa yields a good correlation for all experiments in the range 5–75 GPa (Fig. 4). Ni and Co partitioning have been shown to display a stronger pressure dependence at few GPa, followed by a weaker dependence above 5 GPa, and this has been assigned to a transition in the structure of the melts (Kegler et al., 2008; Sanloup et al., 2011). Although this phenomenon is not critical in our case because the process of core formation occurs for the most part at high pressure, it justifies our choice of neglecting data below 5 GPa. The

experimental data between 5 and 75 GPa can be fit to a single regression for each element (one standard deviation shown in parentheses):

$$\log K_D^{\text{Ni}} = 0.098(0.161) + \frac{3605(342)}{T} - \frac{57(5) \cdot P}{T} \quad (3)$$

$$\log K_D^{\text{Co}} = 0.267(0.115) + \frac{1744(293)}{T} - \frac{37(5) \cdot P}{T} \quad (4)$$

The magnitude of the pressure effect (parameter c in Eq. (2)) for both elements is roughly 25% lower than predicted from previous extrapolations, whereas the magnitude of the temperature effect is in good agreement with previous work (Table 4 provides a review of partitioning parameterizations according to Eq. (2)).

Using our regressions, we calculate the conditions of pressure and temperature that mutually satisfy the apparent bulk core–mantle partition coefficients (D_i) for Ni and Co with the following expression:

$$P = \frac{T}{c} \cdot \left[\log D_i - a + \frac{n}{2} \log \left(\frac{X_{\text{FeO}}^{\text{silicate}}}{X_{\text{Fe}}^{\text{metal}}} \right) \right] - \frac{b}{c} \quad (5)$$

Taking the current FeO content of the mantle ~8 wt.% based on upper-mantle derived rocks (massif peridotites and xenoliths) and chondritic abundances (Allège et al., 1995; McDonough, 2003; Palme and O'Neill, 2003) and a core containing 85 wt.% Fe, the f_{O_2} is constrained during a single-stage core formation event to approximately IW-2.3. To assess in the most precise manner the full range of possible solutions to Eq. (5), we propagated the uncertainties using Monte-Carlo simulations. Ten million (10^7) values of the parameters on the right-hand side of Eq. (5) (partition coefficients D_i , and regression coefficients a , b , c) were generated with a uniform random distribution within their respective error bars. Pressure distributions were then calculated at each temperature, generating an effective statistical set, from which we derived the 1σ uncertainties on P – T solutions to Eq. (5). These are shown in Fig. 6a as red (Ni) and blue (Co) bands. To satisfy the rheological constraint requiring a solid base of the magma ocean to enable ponding of molten metal and final metal–silicate equilibration, the P – T solution domain has to lie between the solidus and liquidus of the mantle. The intersection is represented in yellow in Fig. 6a and represents the locus of possible solutions to a single-stage core-forming event. Pressures lie between 45 and 58 GPa, corresponding to a final depth for the magma ocean of 1150 to 1400 km (Fig. 6a).

The most realistic core-formation model from the point of view of accretionary dynamics involves a process where the core grows sporadically at a rate determined by the discrete pulses of accretion. These models, though perhaps more realistic than single-stage core formation have many degrees of freedom, such as partial equilibration, planetesimal size distribution, mass vs. time distribution, etc. As such, a single-stage P – T constraint can be seen as the average P – T conditions of a series of magma oceans generated from episodic accretion events, including giant impacts.

Continuous core formation, in which the core grows continuously and constantly from 0 to full planetary mass over the course of accretion, is a more realistic model than single-stage core formation (Wade and Wood, 2005). Even if it lacks the realism of episodic accretion, it has the advantage of being simpler to model, and enjoys a small number of degrees of freedom. In this model, the P – T conditions at the base of the magma ocean, still constrained by the peridotite solidus–liquidus, vary (increase) as the Earth grows. Enhancing on the model by Wade and Wood (2005), accretion is modeled in 1000 steps (0.1% constant mass increment per step),

Table 4
Summary of regression coefficients for Ni and Co determined from superliquidus metal–silicate partitioning experimental studies.

Element	a	\pm	b	\pm	c	\pm
Ni						
This work	0.098	0.161	3605	342	−57	5
Gessmann and Rubie (2000)	0.78	0.23	1657	543	−66	6
Li and Agee (2001)	1.35	—	2558	—	−81	—
Chabot et al. (2005)	0.18	0.02	3600	630	−68	4
Wade and Wood (2005)	0.64	—	3097 ^a	—	−123	9
Corgne et al. (2008)	0.50	—	3100 ^a	—	−78	5
Kegler et al. (2008) + lit. (> 5 GPa)	0.26	0.21	3284	453	−74	8
Siebert et al. (2011)	0.35	0.07	2934	279	−83	17
Co						
This work	0.267	0.115	1744	293	−37	5
Gessmann and Rubie (2000)	0.17	0.26	1169	601	−34	8
Li and Agee (2001)	0.11	—	3046	—	−30	—
Chabot et al. (2005)	0.33	0.02	1702	378	−31	3
Wade and Wood (2005)	0.01	—	2511 ^a	—	−45	11
Kegler et al. (2008) + lit. (> 5 GPa)	0.30	0.18	1405	369	−40	7
Siebert et al. (2011)	0.20	0.03	1892	238	−66	8

^a Regression constants are derived from the free energy data

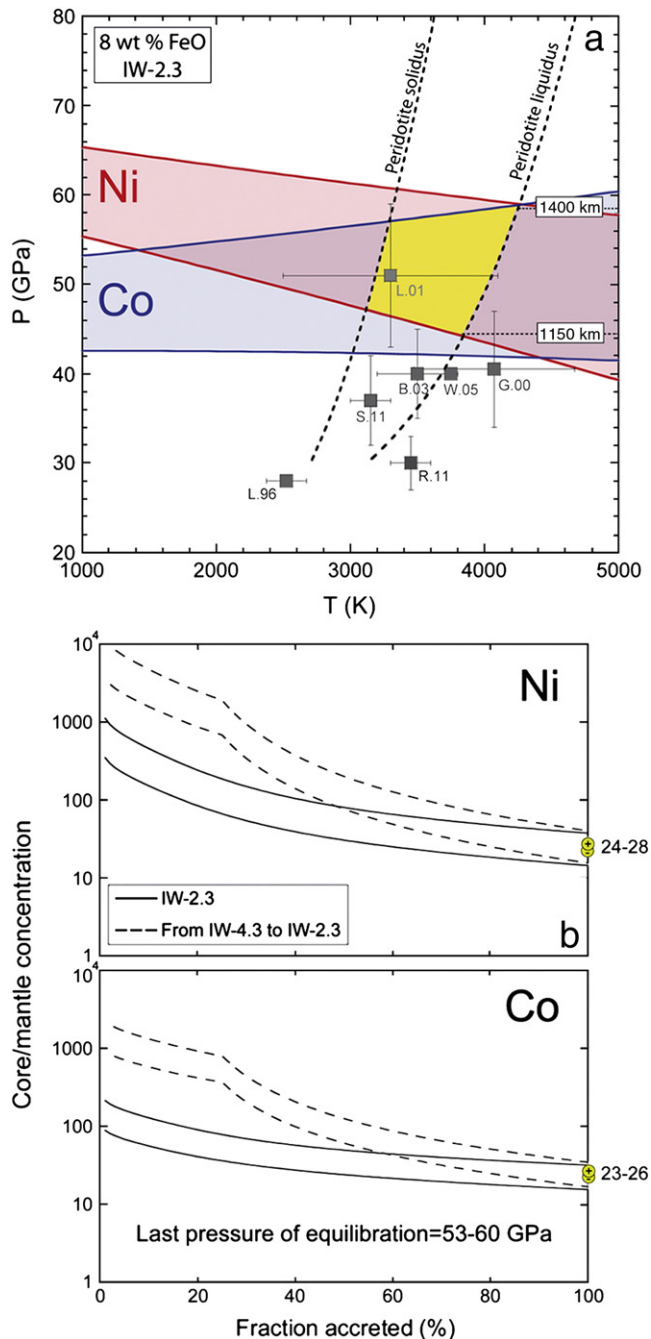


Fig. 6. (a) Diagram showing the P–T conditions of core–mantle equilibration required to match the present-day mantle concentrations of Ni and Co during a single-stage core formation at IW-2.3 (the f_{O_2} is fixed by the present FeO content of the mantle). The individual solutions for Ni (red) and Co (blue) are calculated using regression models (Eqs. (3) and (4)) taking into account the uncertainties on the regression constants and target core–mantle partition coefficients values (10^7 samplings at each temperature using the Monte Carlo method). The solution domain is further constrained to lie within the mantle solidus–liquidus interval (yellow) and provides an upper and lower bound for the depth of the magma ocean. Square symbols are the P–T solutions proposed from previous works (B.03: Bouhifd and Jephcoat, 2003; G.00: Gessmann and Rubie, 2000; L.96: Li and Agee, 1996; L.01: Li and Agee, 2001; R.11: Richter, 2011; S.11: Siebert et al., 2011; W.05: Wade and Wood, 2005). Li and Agee (2001) are in good agreement with our solution domain while other solutions are mostly below the required pressure. (b) Evolution of Ni and Co partition coefficients during continuous core formation in a deep magma ocean. Upper and lower limits for the terrestrial target values are represented by the yellow “+” and “–” symbols. The solid lines show the evolution as a function of accretion (and depth) at constant oxygen fugacity (IW-2.3). The dashed lines are results for models with increasing oxygen fugacity following Wood et al. (2008). Required partitioning values for Ni and Co are matched in both cases, with a final equilibration (100% accretion) taking place around 53–60 GPa (see text).

where the metal is equilibrated with the accumulating mantle and separated after each step. One parameter of the model is the final depth of the magma ocean, and we have run continuous accretion models ranging from 0 (surface magma ocean) to 135 GPa (deepest possible magma ocean, at present day CMB depth). We find that the model that best fits the observed data has a maximum pressure for the magma ocean between 53 and 60 GPa (Fig. 6b). We have run the model with 3 different geotherms to gauge the effect of temperature on our conclusions: along the peridotite solidus, the liquidus, and an intermediate (average) temperature profile. The effects are fairly negligible. Along the liquidus, the terminal magma ocean pressure for core–mantle equilibrium is 56 ± 3 GPa (4100 K). It increases to 58 ± 2 GPa along the intermediate geotherm (3700 K) and to 59 ± 2 GPa following the solidus of peridotite (3300 K). Equilibration pressure slightly increases as the temperature drops, another sign that Ni and Co become more lithophile with increasing pressure and temperature.

Wade and Wood (2005) have argued that initial accretionary material had to be highly reduced, with subsequent gradual oxidation, eventually reaching the present-day terrestrial redox of IW-2.3, in order to reproduce the observed mantle concentrations of slightly siderophile elements like vanadium. We have therefore considered two f_{O_2} paths (FeO content of the silicate melt) during accretion. In the first case, the simplest scenario is considered, where the FeO content of the mantle is constant and equal to its current value (8 wt.%), yielding a f_{O_2} of about IW-2.3. In the second case, accretion starts with reducing material and conditions become progressively oxidizing; the initial FeO mantle content is 0.8 wt.% during the first 25% of accretion (until perovskite becomes stable), and then gradually increases to reach current core–mantle equilibrium value (8 wt.%) at the end of accretion. Both f_{O_2} paths produce the target mantle concentrations for Ni and Co (Fig. 6b) at identical pressures, showing that final Ni and Co partitioning values with this model are fairly independent on redox conditions during accretion.

In a single-stage core-formation event occurring between 45 and 58 GPa and 3200 and 4200 K (solidus/liquidus of peridotite), and at the present-day oxygen fugacity of core–mantle equilibrium (IW-2.3), we find that the core-forming metal contains 1 to 2 wt.% oxygen, and 2 to 13 wt.% silicon (Fig. 5). The seismologically required 5–10% core density deficit (Anderson and Isaak, 2002) can only be obtained above 3500 K, emphasizing the need for a deep magma ocean. For instance, at 3600 K and 53 GPa (the barycentre of our single-stage nickel and cobalt solution domain, Fig. 6a), we produce a core containing 1.3 wt.% oxygen and 6 wt.% silicon, consistent with a 6% core density deficit following the approach taken in Poirier (1994) and Anderson and Isaak (2002). These conditions satisfy both the geochemical constraints for concentration of Ni and Co in mantle-derived rocks, and the geophysical requirement for a core-density deficit due to light-element incorporation in the molten metal.

Acknowledgments

The research leading to these results has received funding from the European Research Council under the European Community's Seventh Framework Programme (FP7/2007–2013)/ERC grant agreement no 207467. This work was performed under the auspices of the US Department of Energy, Lawrence Livermore National Laboratory under Contract DE-AC52-07NA27344 and supported by the Office of Basic Energy Sciences, Geosciences Research Program (FJR). The Focused Ion Beam (FIB) facility of the IMPMC is supported by Région Ile de France grant SESAME 2006 No I-07-593/R, INSU-CNRS, Institut de Physique (INP)–CNRS, University Pierre et Marie Curie–Paris 6, and by the French National Research Agency (ANR) grant ANR-07-BLAN-0124-01. We also thank Imène Esteve for assistance during sample preparation with the FIB. We thank T. M. Harrison for editorial

handling and M.J. Walter for helpful comments that improved the manuscript.

References

- Allègre, C.J., Poirier, J.P., Humler, E., Hofmann, A.W., 1995. The chemical composition of the Earth. *Earth Planet. Sci. Lett.* 134, 515–526.
- Anderson, O.L., Isaak, D.G., 2002. Another look at the core density deficit of Earth's outer core. *Phys. Earth Planet. Inter.* 131, 19–27.
- Andraut, D., Fiquet, G., Itie, J.P., Richet, P., Gillet, P., Hausermann, D., Hanfland, M., 1998. Thermal pressure in a laser-heated diamond-anvil cell: an X-ray diffraction study. *Eur. J. Mineral.* 10, 931–940.
- Andraut, D., Bolfan-Casanova, N., Lo Nigro, G., Bouhifd, M.A., Garbarino, G., Mezouar, M., 2011. Solidus and liquidus profiles of chondritic mantle: implication for melting of the Earth across its history. *Earth Planet. Sci. Lett.* 304, 251–259.
- Antonangeli, D., Siebert, J., Badro, J., Farber, D.L., Fiquet, G., Morard, G., Ryerson, F.J., 2010. Composition of the Earth's inner core from high-pressure sound velocity measurements in Fe–Ni–Si alloys. *Earth Planet. Sci. Lett.* 295, 292–296.
- Armstrong, J.T., 1995. CITZAF—a package of correction programs for the quantitative electron microbeam X-ray analysis of thick polished materials, thin films, and particles. *Microbeam Anal.* 4, 177–200.
- Auzende, A.L., Gillot, J., Coquet, A., Hennet, L., Ona-Nguema, G., Bonnin, D., Esteve, I., Roskosz, M., Fiquet, G., 2011. Synthesis of amorphous MgO-rich peridotitic starting material for laser-heated diamond anvil cell experiments — application to iron partitioning in the mantle. *High pressure Res.* 31, 199–213.
- Benedetti, L.R., Loubeyre, P., 2004. Temperature gradients, wavelength-dependent emissivity, and accuracy of high and very-high temperatures measured in the laser-heated diamond anvil cell. *High pressure Res.* 24, 423–445.
- Boehler, R., 2000. High-pressure experiments and the phase diagram of lower mantle and core materials. *Rev. Geophys.* 38, 221–245.
- Bouhifd, M.A., Jephcoat, A.P., 2003. The effect of pressure on partitioning of Ni and Co between silicate and iron-rich metal liquids: a diamond-anvil cell study. *Earth Planet. Sci. Lett.* 209, 245–255.
- Bouhifd, M.A., Jephcoat, A.P., 2011. Convergence of Ni and Co metal–silicate partition coefficients in the deep magma–ocean and coupled silicon–oxygen solubility in iron melts at high pressures. *Earth Planet. Sci. Lett.* 307, 341–348.
- Brenan, J.M., McDonough, W.F., 2009. Core formation and metal–silicate fractionation of osmium and iridium from gold. *Nature Geosci.* 2, 798–801.
- Capobianco, C.J., Drake, M.J., De'Aro, J., 1999. Siderophile geochemistry of Ga, Ge, and Sn: Cationic oxidation states in silicate melts and the effect of composition in iron–nickel alloys. *Geochim. Cosmochim. Acta* 63, 2667–2677.
- Chabot, N.L., Draper, D.S., Agee, C.B., 2005. Conditions of Earth's core formation: constraints from nickel and cobalt partitioning. *Geochim. Cosmochim. Acta* 69, 2141–2151.
- Corgne, A., Liebske, C., Wood, B.J., Rubie, D.C., Frost, D.J., 2005. Silicate perovskite–melt partitioning of trace elements and geochemical signature of a deep perovskitic reservoir. *Geochim. Cosmochim. Acta* 69, 485–496.
- Corgne, A., Keshav, S., Wood, B.J., McDonough, W.F., Fei, Y., 2008. Metal–silicate partitioning and constraints on core composition and oxygen fugacity during Earth accretion. *Geochim. Cosmochim. Acta* 72, 574–589.
- Corgne, A., Siebert, J., Badro, J., 2009. Oxygen as a light element: a solution to single-stage core formation. *Earth Planet. Sci. Lett.* 288, 108–114.
- Fiquet, G., Auzende, A.L., Siebert, J., Corgne, A., Bureau, H., Ozawa, H., Garbarino, G., 2010. Melting of peridotite to 140 gigapascals. *Science* 329, 1516–1518.
- Frost, D.J., Asahara, Y., Rubie, D.C., Miyajima, N., Dubrovinsky, L.S., Holzapfel, C., Ohtani, E., Miyahara, M., Sakai, T., 2010. The partitioning of oxygen between the Earth's mantle and core. *J. Geophys. Res.* 115, B02202.
- Gessmann, C.K., Rubie, D.C., 2000. The origin of the depletions of V, Cr and Mn in the mantles of the Earth and Moon. *Earth Planet. Sci. Lett.* 184, 95–107.
- Halliday, A.N., Wood, B.J., 2009. How did Earth accrete? *Science* 325, 44–45.
- Hilgren, V.J., Drake, M.J., Rubie, D.C., 1996. High pressure and high temperature metal–silicate partitioning of siderophile elements: the importance of silicate liquid composition. *Geochim. Cosmochim. Acta* 60, 2257–2263.
- Holzheid, A., Sylvester, P., O'Neill, H., St, C., Rubie, D.C., Palme, H., 2000. Evidence for a late chondritic veneer in the Earth's mantle from high-pressure partitioning of palladium and platinum. *Nature* 406, 396–399.
- Ito, E., et al., 1995. Reaction between molten iron and silicate melts at high pressure: implications for the chemical evolution of the Earth's core. *J. Geophys. Res.* 100, 5901–5910.
- Jana, D., Walker, D., 1997. The influence of silicate melt composition on distribution of siderophile elements among metal and silicate liquids. *Earth Planet. Sci. Lett.* 150, 463–472.
- Japan Society and for the Promotion of Science and the Nineteenth Committee on Steelmaking, 1988. *Steelmaking Data Sourcebook*. Gordon and Breach Science Publishers, New York. 273–297 pp.
- Kegler, P., Holzheid, A., Frost, D.J., Rubie, D.C., Dohmen, R., Palme, H., 2008. New Ni and Co metal–silicate partitioning data and their relevance for an early terrestrial magma ocean. *Earth Planet. Sci. Lett.* 268, 28–40.
- Li, J., Agee, C.B., 1996. Geochemistry of mantle–core differentiation at high pressure. *Nature* 381, 686–689.
- Li, J., Agee, C.B., 2001. The effect of pressure, temperature, oxygen fugacity and composition on the partitioning of nickel and cobalt between liquid Fe–Ni–S alloy and liquid silicate: implications for the Earth's core formation. *Geochim. Cosmochim. Acta* 65, 1821–1832.
- Lord, O.T., Walter, M.J., Dasgupta, R., Walker, D., Clark, S.M., 2009. Melting in the Fe–C system to 70 GPa. *Earth Planet. Sci. Lett.* 284, 156–167.
- Mann, U., Frost, D.J., Rubie, D.C., 2009. Evidence for high-pressure core–mantle differentiation from the metal–silicate partitioning of lithophile and weakly-siderophile elements. *Geochim. Cosmochim. Acta* 73, 7360–7386.
- Matsui, T., Abe, Y., 1986. Formation of a “magma ocean” on the terrestrial planets due to the blanketing effect of an impact induced atmosphere. *Earth Moon Planets* 34, 223–230.
- McDonough, W.F., 2003. Compositional model for the Earth's core. In: Carlson, R.W. (Ed.), *Treatise on Geochemistry*, vol. 2. Elsevier–Pergamon, Oxford, pp. 547–568.
- Nomura, R., Ozawa, H., Tateno, S., Hirose, K., Hernlund, J., Muto, S., Ishii, H., Hiraoka, N., 2011. Spin crossover and iron-rich silicate melt in the Earth's deep mantle. *Nature* 473, 199–202.
- Ohtani, E., Yurimoto, H., Seto, S., 1997. Element partitioning between metallic liquid, silicate liquid, and lower-mantle minerals: implications for core formation of the Earth. *Phys. Earth Planet. Inter.* 100, 97–114.
- O'Neil, H.St.C., Canil, D., Rubie, D.C., 1998. Oxide–metal equilibria to 2500°C and 25 GPa: implications for core formation and the light component in the Earth's core. *J. Geophys. Res.* 103, 12239–12260.
- Palme, H., O'Neill, H., St, C., 2003. Cosmochemical estimates of mantle composition. In: Carlson, R.W. (Ed.), *Treatise on Geochemistry*, vol. 2. Elsevier–Pergamon, Oxford, pp. 1–38.
- Poirier, J.P., 1994. Light elements in the Earth's core: a critical review. *Phys. Earth Planet. Inter.* 85, 319–337.
- Ricolleau, A., Fei, Y.W., Cottrell, E., Watson, H., Deng, L.W., Zhang, L., Fiquet, G., Auzende, A.L., Roskosz, M., Morard, G., Prakapenka, V., 2009. Density profile of pyrolite under the lower mantle conditions. *Geophys. Res. Lett.* 36, L06302.
- Ricolleau, A., Fei, Y.W., Corgne, A., Siebert, J., Badro, J., 2011. Constraints on oxygen and silicon contents of Earth's core from metal–silicate partitioning experiments at high pressure and temperature. *Earth Planet. Sci. Lett.* 310, 409–421.
- Righter, K., Drake, M.J., Yaxley, G., 1997. Prediction of siderophile element metal–silicate partition coefficients to 20 GPa and 2800°C: the effects of pressure, temperature, oxygen fugacity and silicate and metallic melt compositions. *Phys. Earth Planet. Inter.* 100, 115–134.
- Righter, K., 2011. Prediction of metal–silicate partition coefficients for siderophile elements: an update and assessment of PT conditions for metal–silicate equilibrium during accretion of the Earth. *Earth Planet. Sci. Lett.* 304, 158–167.
- Safronov, S.V., 1978. Heating of Earth during its formation. *Icarus* 33, 3–12.
- Sanloup, C., van Westrenen, W., Dasgupta, R., Maynard-Casely, H., Perrillat, J.P., 2011. Compressibility change in iron-rich melt and implications for core formation models. *Earth Planet. Sci. Lett.* 306, 118–122.
- Siebert, J., Corgne, A., Ryerson, F.J., 2011. Systematics of metal–silicate partitioning for many siderophile elements applied to Earth's core formation. *Geochim. Cosmochim. Acta* 75, 1451–1489.
- Stevenson, D.J., 1990. Fluid dynamics of core formation. In: Newsom, H., Jones, J.H. (Eds.), *The Origin of the Earth*. Oxford Press, London, pp. 231–249.
- Thibault, Y., Walter, M.J., 1995. The influence of pressure and temperature on the metal–silicate partition coefficients of nickel and cobalt in a model C1 chondrite and implications for metal segregation in a deep magma ocean. *Geochim. Cosmochim. Acta* 59, 991–1002.
- Tonks, W.B., Melosh, H.J., 1993. Magma ocean formation due to giant impacts. *J. Geophys. Res.* 98, 519–5333.
- Wade, J., Wood, B.J., 2001. The Earth's missing niobium may be in the core. *Nature* 409, 75–78.
- Wade, J., Wood, B.J., 2005. Core formation and the oxidation state of the Earth. *Earth Planet. Sci. Lett.* 236, 78–95.
- Wood, B.J., Wade, J., Kilburn, M.R., 2008. Core formation and the oxidation state of the Earth: additional constraints from Nb, V and Cr partitioning. *Geochim. Cosmochim. Acta* 72, 1415–1426.